Ultra-fast spin dynamics in the 2s2p^2 configuration of C^+ studied by time-dependent R-matrix theory

Hutchinson, S., Lysaght, M. A., & Van Der Hart, H. (2011). Ultra-fast spin dynamics in the 2s2p^2 configuration of C^+ studied by time-dependent R-matrix theory. Journal of Physics B: Atomic Molecular and Optical Physics, 44(21), 215602. [215602]. DOI: 10.1088/0953-4075/44/21/215602

Published in:
Journal of Physics B: Atomic Molecular and Optical Physics

Document Version:
Early version, also known as pre-print

Ultra-fast spin dynamics in the $2s2p^2$ configuration of C^+ studied by time-dependent R-matrix theory

Steven Hutchinson[1], Michael A. Lysaght[1,2] and Hugo W. van der Hart[1]

[1] Centre for Theoretical Atomic, Molecular and Optical Physics, Queen's University Belfast, Belfast BT7 1NN, United Kingdom
[2] Department of Physics and Astronomy, The Open University, Walton Hall, Milton Keynes, MK7 6BJ, United Kingdom

E-mail: shutchinson06@qub.ac.uk

Abstract. We employ time-dependent R-matrix theory to study ultra-fast dynamics in the doublet $2s2p^2$ configuration of C^+ for a total magnetic quantum number $M = 1$. In contrast to the dynamics observed for $M = 0$, ultra-fast dynamics for $M = 1$ is governed by spin dynamics in which the 2s electron acts as a flag rather than a spectator electron. Under the assumption that $m_S = 1/2$, $m_{2s} = 1/2$ allows spin dynamics involving the two 2p electrons, whereas $m_{2s} = -1/2$ prevents spin dynamics of the two 2p electrons. For a pump-probe pulse scheme with $\hbar\omega_{\rm pump} = 10.9$ eV and $\hbar\omega_{\rm probe} = 16.3$ eV and both pulses six cycles long, little sign of spin dynamics is observed in the total ionization probability. Signs of spin dynamics can be observed, however, in the ejected-electron momentum distributions. We demonstrate that the ejected-electron momentum distributions can be used for unaligned targets to separate the contributions of initial $M = 0$ and $M = 1$ levels. This would, in principle, allow unaligned target ions to be used to obtain information on the different dynamics in the $2s2p^2$ configuration for the $M = 0$ and $M = 1$ levels from a single experiment.

PACS numbers: 32.80.Rm,31.15.A-,32.80.Qk

† Steven Hutchinson, Michael A. Lysaght and Hugo W. van der Hart, *J. Phys. B: At. Mol. Opt. Phys.* **44**, 215602 (2011).

1. Introduction

Recent developments in the generation of ultra-short light pulses have opened up the possibility to study atomic and molecular processes on a sub-femtosecond timescale. Examples of the types of dynamics investigated experimentally on this timescale include the decay of autoionizing states [1], the vibrational dynamics of hydrogen molecules [2], the dynamics of shake-up states during VUV photoionization [3], correlated-electron dynamics in small molecules [4] and the relative time delay of photoionization processes [5]. Via the Heisenberg uncertainty principle, electron dynamics within atoms can be seen as the complement of atomic structure. Ultra-short light pulses thus provide an entirely new way of looking at atoms and atomic interactions.

The experimental developments need to be matched by developments in theory. Theoretical atomic physics approaches have put great emphasis on the accurate inclusion of electron-electron interactions to describe atomic structure in great accuracy. However, until now, relatively little emphasis has been given to the dynamical interpretation of atomic structure. The reason for this is that a theoretical description of dynamics including electron-electron interactions has proven to be difficult since it requires a full, time-dependent multi-electron approach. Typical theoretical methods describe systems limited to a maximum of two active electrons, possibly outside a closed core [6, 7]. The ultra-fast multi-electron dynamics of current interest cannot be described in full detail even by these sophisticated approaches. Very few methods, such as presented in [8], are capable of describing strongly correlated electron interactions on an ultrafast timescale in general systems with more than two active electrons. A complete picture of multi-electron dynamics can hence only be obtained by general-atom codes.

A major advance in the description of general multi-electron atomic dynamics in intense light has been made recently through the development of Time-Dependent R-matrix (TDRM) theory [9, 10]. The theory combines a time-dependent propagation of the wavefunction with the highly successful R-matrix approach for scattering processes [11]. Although the initial approach investigated systems confined within the R-matrix inner region, subsequent developments employ the standard R-matrix approach of separating space into an inner region and an outer region [12, 13]. In these recent code developments, all interactions between all electrons are included for the inner region, whereas in the outer region the outer electron only feels the long-range interactions from the nucleus and remaining electrons and the light field. An outer-region approach based on R-matrix propagation techniques [12] has already been applied successfully to describe two-photon ionization of Neon [14] and ultrafast dynamics of a $2s2p^2$ wavepacket in C^+ [15, 16, 17]. More recently, R-matrix inner region techniques have been combined with an outer-region approach which employs a finite-difference approach to obtain the R-matrix with time dependence (RMT) approach [13, 18].

Time-dependent R-matrix theory has in particular been applied to investigate ultra-fast dynamics in C^+, with a particular emphasis on demonstrating how electron-electron repulsion can drive ultra-fast dynamics: through a pump-probe pulse scheme, oscillations in the ionization probability of C^+ were observed due to dynamics within the $2s2p^2$ configuration [15]. As the states driving the dynamics are confined to a single configuration, the only interaction which can drive the wavepacket dynamics is electron-electron repulsion. For C^+ initially in the $2s^22p$ ground state with $M = 0$, the wavepacket dynamics is confined to spatial dynamics. Momentum distributions

of the ejected electron provided even clearer evidence that the dynamics consists of the simultaneous transfer of population from two 2p electrons with $m = 0$ to two 2p electrons with $|m| = 1$ and vice versa [16]. Finally, we demonstrated that the pump pulse length is a critical parameter for the observation of dynamics [17]. We note that features of high-harmonic spectra obtained from molecules have been assigned to correlated-electron dynamics [4, 19]. Work is currently underway to develop theoretical understanding of these molecular effects through 2D models for diatomic molecules [20]. At present, our focus is on developing understanding of correlated-electron dynamics within atoms through application of TDRM theory.

One of the limitations of the previous work on the dynamics in C^+ was its limitation to initial states with $M = 0$. In the present study, we address this limitation by investigating the dynamics obtained for this pump-probe scheme when the initial C^+ ground state has $M \neq 0$. For a $^2P^o$ state, this means that we need to consider $M = 1$. In general, the dynamics of systems with $M = 1$ has not been investigated as thoroughly as $M = 0$, even though the dynamics in $M = 0$ and the dynamics in $M = 1$ may differ at a fundamental level, as we will show shortly. The exploration of dynamics involving states with $M = 1$ requires some important modifications to the time-dependent R-matrix codes. Most importantly, for $M = 1$, additional symmetries such as $^2P^e$ and $^2D^o$ need to be included in the calculations. These symmetries played no role in the calculations carried out for $M = 0$. As a consequence of these additional symmetries, not only can we expect dramatic changes in the dynamics, the calculations also increase substantially in size.

Although most targets considered in atomic physics experiments are noble-gas-like atoms, which have $M = 0$ due to the filled valence shell, it is still important to develop the capability to investigate systems with $M = 1$ efficiently. Comparisons with experiments performed on unaligned systems with non-zero total angular momentum are only possible if theory accounts for initial states with non-zero M. This will, for example, be the case for most complex multi-electron targets with open valence shells, such as the C^+ ion. Thus, by combining results obtained for both $M = 0$ and $M = 1$ initial states of C^+, we can predict the response of an unaligned target to ultrafast, linearly polarized light pulses. These predictions for an unaligned target should provide a better comparison with experimental setups. In addition, by comparing the contributions from both $M = 0$ and $M = 1$ initial states, we may find ways to distinguish the contribution from each in an unaligned target.

In this paper, we investigate the dynamics of a 2s2p^2 electron wavepacket in the C^+ ion when the ion is initially in the $M = 1$ level of the 2s^{2}2p ground state. We use the same pump-probe scheme as our earlier studies for C^+ initially in the $M = 0$ level as well as a pump-probe scheme with laser energies chosen to optimize $M = 1$ dynamics. We study both the ionization probability and 2D momentum distributions to observe features showing signs of spin dynamics. Furthermore, we combine the present results with those obtained previously for $M = 0$ to investigate the response of an unaligned target. We start, however, with a brief overview of time-dependent R-matrix theory and the changes between the approach for $M = 0$ and $M \neq 0$.

2. Time Dependent R-Matrix Theory

Throughout this study we use the time dependent R-matrix theory to study the evolution of C^+ in time. Time-dependent R-matrix theory extends standard R-matrix methods for scattering processes to time-dependent processes induced by ultra-short

light pulses. A thorough overview of this theory has been published previously [12] and as such only a brief description will be given here.

The TDRM method solves the time-dependent Schrödinger equation for a general (N+1)-electron atom or ion interacting with a light field by making use of the unitary Cayley form of the time evolution operator to express the TDSE in the form of a Crank-Nicolson scheme as follows:

$$(H(t_{q+\frac{1}{2}}) - E)\Psi(\mathbf{X}_{N+1}, t_{q+1}) = \Theta(\mathbf{X}_{N+1}, t_q), \tag{1}$$

where

$$\Theta(\mathbf{X}_{N+1}, t_q) = -(H(t_{q+\frac{1}{2}}) + E)\Psi(\mathbf{X}_{N+1}, t_q). \tag{2}$$

In equations (1) and (2), $\mathbf{X}_{N+1} \equiv \mathbf{x}_1, \mathbf{x}_2, \ldots, \mathbf{x}_{N+1}$, where $\mathbf{x}_i \equiv \mathbf{r}_i\sigma_i$ are the space and spin coordinates of the i^{th} electron and Ψ is the time-dependent wavefunction. $H(t_{q+\frac{1}{2}})$ is the time-dependent Hamiltonian at the midpoint of times t_q and t_{q+1}. The imaginary energy E is defined by the time step $\Delta t = t_{q+1} - t_q$ and is given by $E \equiv 2i\Delta t^{-1}$. Throughout this paper the light field is assumed to be spatially homogeneous and linearly polarized. Previous work has shown that the optimum choice of gauge for this type of problem is the length gauge [21], thus the Hamiltonian is described using the length gauge throughout.

The solution to (1) follows the same methods employed in standard R-matrix theory by partitioning the configuration space into an internal region with radius $r = a_0$ and an external region [11]. The internal region contains all $(N + 1)$ electrons and considers all exchange and correlation effects between these electrons. The external region contains only the outer or ejected electron, which is acted upon only by the long range potential of the residual N-electron atom or ion and the laser field in this region.

In the internal region we use an R-Matrix basis expansion, ψ_k, of the wave function to describe the $(N + 1)$ electron system. After the addition of a Bloch operator to ensure Hermicity at the boundary $r = a_0$, we may then re-write (2) as:

$$(H + \mathcal{L} - E)\Psi_{q+1} = \mathcal{L}\Psi_{q+1} + \Theta_q \tag{3}$$

with formal solution

$$\Psi = (H + \mathcal{L} - E)^{-1}\mathcal{L}\Psi + (H + \mathcal{L} - E)^{-1}\Theta. \tag{4}$$

Solutions to this equation can be found by expressing the full time-dependent wavefunction in the inner region in terms of inner-region eigenfunctions ψ_k of the operator $(H + \mathcal{L})$:

$$\Psi(\mathbf{X}_{N+1}, t_{q+1}) = \Sigma_k \psi_k(\mathbf{X}_{N+1}) B_k(E, t_{q+1}) \tag{5}$$

where B_k are time-dependent expansion coefficients.

In order to connect the inner-region with the outer-region wavefunctions, a relation between the wavefunction and its first derivative needs to be obtained at the inner-region boundary. We project (4) onto the n time-independent channel functions $\bar{\Phi}_p^{\gamma}$, which are formed by coupling the residual ion state Φ with the angular and spin functions of the continuum electron. Evaluating the resulting expression on the internal region boundary $r_{N+1} = a_0$, we obtain in matrix notation an expression of the form:

$$\mathbf{F}(a_0) = \mathbf{R}a_0\bar{\mathbf{F}}(a_0) + \mathbf{T}(a_0), \tag{6}$$

where the vector $\mathbf{F}$ indicates the wavefunction of the continuum, $\bar{\mathbf{F}}$ its first derivative and $\mathbf{R}$ and $\mathbf{T}$ the so-called R-matrix and T-vector respectively. This form of (6) is similar to the form obtained in standard R-matrix techniques for scattering [11], with $\mathbf{R}a_0\bar{F}(a_0)$ originating from the first term of the right-hand side in (4) and $\mathbf{T}(a_0)$ originating from the second term on the right-hand side. The R-Matrix and T-vector provide information about the rate of flow of the wavefunction through the inner region boundary at time $t = t_{q+1}$ and time $t = t_q$, respectively. Once we obtain the vector $\mathbf{F}$, we can determine the coefficients B_k and consequently the full wavefunction Ψ in the internal region. However, to determine the first derivative $\bar{\mathbf{F}}$ we must consider the external region.

Within the external region, the wavefunction is expanded as:

$$\Psi(\mathbf{X}_{N+1}, t_{q+1}) = \sum_{p=1}^{n} \bar{\Phi}_p^{\gamma}(\mathbf{X}_N; \hat{\mathbf{r}}_{N+1}) r_{N+1}^{-1} F_p(r_{N+1}) \tag{7}$$

where the reduced radial functions F_p are analytic continuations of the functions defined on the inner region boundary in (6). The outer region is divided into subsectors, spanning from the inner region boundary out to a distance where the wavefunction can be assumed to vanish during the entire calculation. Following similar techniques to those used for the inner region, and detailed in [12], it is possible to ensure that the external region Hamiltonian is Hermitian at the boundaries of each subsector with a formal solution in a form similar to that of (4). From this, as demonstrated explicitly in [12], we obtain at each subsector boundary an equation which is similar in form to (6).

With this information, it is possible to develop an approach which can determine the vector $\mathbf{F}$ and its first derivative $\bar{\mathbf{F}}$ in the outer region. Using the Hamiltonian on each subsector, we can propagate the R-matrix and T-vector from the inner region boundary $r = a_0$ across the boundaries of every subsector in the external region. The techniques used for this purpose are described in detail in [12]. Since the external region is chosen large enough that the wavefunction will not reach the outermost boundary, the vector $\mathbf{F}$ can be assumed to remain equal to zero at the outer boundary. Using this initial condition, in conjunction with the R-matrix and T-vector propagated outwards, $\mathbf{F}$ can be propagated inwards across the subsector boundaries up to the inner region boundary. Once $\mathbf{F}$ is known at all sector boundaries, the wavefunction at $t = t_{q+1}$ can be determined within all regions. This process is then repeated to propagate the wave function through successive time steps.

The ability of the TDRM method to describe the electron exchange potential accurately from first principles represents a significant advantage over methods such as time dependent density functional theory (TDDFT) in the description of multi-electron dynamics on an ultrafast timescale as studied in the present example. In systems such as C^+ where electron exchange drives the underlying electron dynamics, an accurate description of the exchange potential is essential for the description of ultrafast dynamics between discrete electrons. In larger, more complex, systems the dynamics may be more complicated than in the present case. Then the effects of electron exchange will be distributed across all of the electrons. In this case methods tailored to the description of large systems, such as TDDFT may become more applicable. Currently, the TDRM method is limited to describing single electron ionization of an atomic target. Work is proceeding to extend the technique to molecular systems and to the description of multi-electron ionization.

3. Specific Developments for $M = 1$

3.1. Differences in the TDRM approach between $M = 0$ and $M \neq 0$

In this investigation our interest lies in the dynamics in a C^+ ion, initially in the $2s^22p$ state with $|M| = 1$, and how this dynamics compares to the dynamics observed previously for an initial $2s^22p$ state with $M = 0$. The magnetic quantum number M determines which radiative transitions are possible in the system under observation according to the selection rules. In a system with $M = 0$, these selection rules state that for any radiative transition:

$$\Delta L = \pm 1, \qquad \Delta L \neq 0 \tag{8}$$

For a system with $|M| = 1$, the selection rules become

$$\Delta L = \pm 1, \qquad \Delta L = 0 \tag{9}$$

Additionally, requiring $|M| = 1$ prevents the system from having S symmetry. The main change in the selection rules is thus to allow $\Delta L = 0$ transitions. Allowing $\Delta L = 0$ transitions increases the number of symmetries available by allowing both even and odd parity for each angular momentum whereas for $M = 0$ only a single parity needs to be considered for each angular momentum.

The increase in the number of symmetries also significantly increases the computational difficulty of the problem: the size of the Hamiltonian involved increases with the number of symmetries. Moreover, each LS symmetry now interacts typically with three other LS symmetries rather than two. As a consequence, the solution of the relevant linear equations takes significantly longer, particularly when we need to retain many angular momenta, with significantly more memory required to store the relevant matrices. The increased memory demands are kept to a minimum by making use of the banded nature of the Hamiltonian as a result of the selection rules. Naïvely ordering the symmetries in an alternating even and odd parity arrangement results in a banded structure of the form:

$$H = \begin{pmatrix} H_{P^eP^e} & H_{P^eP^o} & 0 & H_{P^eD^o} & 0 & 0 & \ddots \\ H_{P^oP^e} & H_{P^oP^o} & H_{P^oD^e} & 0 & 0 & 0 & \ddots \\ 0 & H_{D^eP^o} & H_{D^eD^e} & H_{D^eD^o} & 0 & H_{D^eF^o} & \ddots \\ H_{D^oP^e} & 0 & H_{D^oD^e} & H_{D^oD^o} & H_{D^oF^e} & 0 & \ddots \\ 0 & 0 & 0 & H_{F^eD^o} & H_{F^eF^e} & H_{F^eF^o} & \ddots \\ 0 & 0 & H_{F^oD^e} & 0 & H_{F^oF^e} & H_{F^oF^o} & \ddots \\ \ddots & \ddots & \ddots & \ddots & \ddots & \ddots & \ddots \end{pmatrix} \tag{10}$$

In this case the band width spans three off-diagonal blocks in the Hamiltonian. We can reduce this by rearranging the symmetries so that the parity ordering alternates

for every angular momentum between even-odd and odd-even as follows:

$$H = \begin{pmatrix} H_{P^eP^e} & H_{P^eP^o} & H_{P^eD^o} & 0 & 0 & 0 & \ddots \\ H_{P^oP^e} & H_{P^oP^o} & 0 & H_{P^oD^e} & 0 & 0 & \ddots \\ H_{D^oP^e} & 0 & H_{D^oD^o} & H_{D^oD^e} & H_{D^oF^e} & 0 & \ddots \\ 0 & H_{D^eP^o} & H_{D^eD^o} & H_{D^eD^e} & 0 & H_{D^eF^o} & \ddots \\ 0 & 0 & H_{F^eD^o} & 0 & H_{F^eF^e} & H_{F^eF^o} & \ddots \\ 0 & 0 & 0 & H_{F^oD^e} & H_{F^oF^e} & H_{F^oF^o} & \ddots \\ \ddots & \ddots & \ddots & \ddots & \ddots & \ddots & \ddots \end{pmatrix}. \quad (11)$$

In this arrangement of angular momenta, the band width spans only two off-diagonal symmetries. This arrangement of the symmetries was chosen for the present calculations.

3.2. M=1 multi-electron dynamics in C$^+$

A change in the initial value of M can have a significant effect on the physics of the system under investigation. The actual effects will depend significantly on the configuration under investigation, so we illustrate this by explaining how the value of M affects the dynamics in the 2s2p^2 configuration of C$^+$. We previously studied the collective dynamics of this configuration for a total magnetic quantum number $M = 0$ using an ultrashort pump-probe scheme. A six-cycle 10.9 eV pump pulse creates a wavepacket in the 2s2p^2 ^{2}D^e and ^{2}S^e states. After a time delay, the C$^+$ ion is ionized by a six-cycle probe pulse. The photon energy of the probe pulse was chosen such that the dynamics was observed through either ionization probabilities [15] or through 2D ejected-electron momentum distributions leaving C^{2+} in the 2s2p ^{3}P state [16]. These observables showed oscillations with a period of 1.5 fs, which matched oscillations in the population of the $|2p_0 2p_0>$ and $|2p_1 2p_{-1}>_S$ states in the uncoupled 2p^2 basis (the subscript S indicates that the two electrons couple to a singlet). This demonstrated that the wavepacket is driven primarily by electron-electron repulsion between the two 2p electrons, and that the dynamics of the 2p electrons is confined to spatial dynamics only. The 2s electron could be considered a spectator electron.

Now, let us consider what will occur if the initial 2s^{2}2p ^{2}P^o state of C$^+$ has M=1. The excitation pulse will again create a superposition of two states in the 2s2p^2 configuration. With $M = 1$, excitation to the ^{2}S^e state is not allowed, but excitation to the ^{2}D^e state is. However, since $\Delta L = 0$ transitions are now allowed, excitation to the ^{2}P^e state is also possible. To reveal the dynamics, we have to investigate the uncoupled basis states. First of all, we need to identify which uncoupled basis states make up the ^{2}P^e and ^{2}D^e states. We will consider angular momentum first. The 2s electron must have $m_\ell = 0$. The 2p electrons can have $m_\ell = -1, 0$ or 1. To obtain a total $M = 1$, the only possibility is that one of the two 2p electrons has $m_\ell = 0$ and the other $m_\ell = 1$. This, however, means that only one combination of m_ℓ values is possible, and hence there can be no spatial dynamics in the 2s2p^2 configuration for $M = 1$.

If there is no dynamics in the spatial part of the 2s2p^2 wavefunction for $M = 1$, then the dynamics must occur in the spin functions. In the absence of the 2s electron, the two 2p electrons couple to a well-defined total spin: either singlet for ^{1}D^e or

triplet for ^{3}P^e. The presence of the additional 2s electron allows these two different spin states to couple to same total spin $S = 1/2$. To understand the dynamics for $M = 1$, the 2s electron can thus no longer be considered a spectator electron: it plays an important role in the dynamics within the 2s2p^2 configuration. In order to explain the role of the 2s electron, it is easiest to transform our basis from LS-coupled states into the uncoupled basis.

The uncoupled basis that we use to illustrate the spin dynamics contains three-electron functions of the form $\mid 2s_0^{\pm}2p_1^{\pm}2p_0^{\pm}\rangle$. If we assume that the initial state originally has $m_s = 1/2$, then we can write the three uncoupled basis functions involved in the dynamics as $\mid 2s_0^{+}2p_1^{+}2p_0^{-}\rangle$, $\mid 2s_0^{+}2p_1^{-}2p_0^{+}\rangle$ and $\mid 2s_0^{-}2p_1^{+}2p_0^{+}\rangle$, which we simplify as $\mid 0^+1^+0^-\rangle$, $\mid 0^+1^-0^+\rangle$ and $\mid 0^-1^+0^+\rangle$, respectively. The first 0 thus indicates the 2s electron, and the second the 2p electron. Note that we have three basis states of this type, whereas we have only two LS states. The $M = 1$ level of the ^{4}P^e state can also be expressed in terms of these uncoupled basis states, but it plays no role in the present work.

If we take a closer look at the uncoupled basis functions, we can see the role that the 2s electron plays in the dynamics. The basis state $\mid 0^-1^+0^+\rangle$ has spin-down for the 2s electron, whereas both 2p electrons have spin-up. But that can only occur if the two 2p electrons couple to form a triplet state. This basis state is thus linked to the 2s2p^2 ^{2}P^e state, but not to the 2s2p^2 ^{2}D^e state. This basis state can thus not be part of dynamics within 2s2p^2. On the other hand, the basis states $\mid 0^+1^-0^+\rangle$ and $\mid 0^+1^+0^-\rangle$ have spin-up for the 2s electron, and one spin-up 2p electron and one spin-down 2p electron. Both basis states are linked to both the 2s2p^2 ^{2}P^e and ^{2}D^e states, and can thus be involved in spin dynamics. The spin of the 2s electron thus acts as a flag for the dynamics. If the 2s electron has $m_s = -M_s$, spin dynamics is not allowed within 2s2p^2, whereas if it has $m_s = M_s$, dynamics is allowed.

It is also of interest to consider how the uncoupled basis states interact with the 2s^{2}2p ground state. In terms of uncoupled basis functions, the ground state has two 2s electrons, $m_\ell = 0, m_s = \pm 1/2$, and one 2p electron $m_\ell = 1, m_s = 1/2$ with the latter condition chosen to match the labels of the uncoupled basis states. Excitation of the ground state to the 2s2p^2 configuration will primarily occur by excitation of one 2s electron to the $m_\ell = 0$ level of the 2p state. Thus states $\mid 0^-1^+0^+\rangle$ and $\mid 0^+1^+0^-\rangle$ will interact strongly with the ground state in a light field, whereas state $\mid 0^+1^-0^+\rangle$ will not. Obviously, population will have to be transferred into $\mid 0^+1^-0^+\rangle$, as it is a essential component of the LS-coupled eigenstates. However, it will receive its population not via excitation from the light pulse, but through electron-electron interactions with states $\mid 0^-1^+0^+\rangle$ and $\mid 0^+1^+0^-\rangle$.

3.3. Application to C$^+$

To describe the structure of C$^+$ in the internal region, we employ the same approach as in the previous study [15]. The inner region is chosen to extend to a radius of 20 au, with the set of continuum orbitals containing 90 continuum functions for each available angular momentum of the continuum electron. The 1s^{2}2s^2 ^{1}S^e ground state and the 1s^{2}2s2p ^{3}P^o and ^{1}P^o excited states of C^{2+} are included as target states. All 1s^{2}2s$^2\epsilon l$ and 1s^{2}2s2pϵl channels with angular momentum up to and including $L_{\max} = 5$ are included in the description of C$^+$. The external region is chosen to extend to a radial distance of 1799 au and is composed of subsectors of width 3 au which contain 35 B-Splines per channel with order $k = 9$. These parameters are used for all calculations

unless otherwise stated.

Extensive calculations are performed using an identical pump probe scheme to our initial studies for $M = 0$. Under this scheme we use a pump laser with a photon energy of $\omega_1 = 10.9$ eV and a duration of 2.28 fs to excite the target into a superposition between the 2s2p^2 ^{2}P^e and ^{2}D^e states, before ionizing the target after a variable delay of δt using an ultrashort probe pulse with photon energy $\omega_2 = 16.3$ eV and a duration of 1.52 fs. These frequencies were originally chosen to excite equally the 2s2p^2 ^{2}S^e and ^{2}D^e states for $M = 0$, however for $M = 1$ there is a large detuning between the pump laser energy of $\omega_1 = 10.9$ eV and the 2s^{2}2p ^{2}P^o-2s2p^2 ^{2}P^e transition energy. Consequently we also investigate a similar pump probe scheme with a pump laser energy of $\omega_1 = 11.5$ eV and duration 2.16 fs to excite the 2s2p^2 ^{2}P^e and ^{2}D^e states equally and enhance the $M = 1$ dynamics. To ensure that our results remain comparable, we use a lower probe pulse energy of $\omega_2 = 15.7$ eV and duration 1.58 fs to ensure the same final energy in both pump probe schemes. In all cases the laser field is linearly polarized in the z direction and described by a three-cycle sin^2 ramp on, followed by a three-cycle sin^2 ramp off. Every laser field has a maximum intensity of 5×10^{12} W cm^{-2}. Throughout all calculation we define the time step as $\Delta t = 0.1$ au, which is approximately 2.42 as.

4. Results

In this section, we present ionization probabilities and ejected-electron momentum distributions for C$^+$ subjected to a sequence of two ultra-short pulses. All ionization probabilities are calculated at approximately 30 fs beyond the end of the probe pulse and represent the probability of an electron being ejected into a space extending from 200 au to 1799 au unless otherwise stated. All momentum distributions are calculated at approximately 30 fs beyond the end of the probe pulse, and are obtained for electrons at distances between 65 and 1799 au from the nucleus.

Figure 1 shows the ionization probability for C$^+$ initially in the ground state with $M = 1$ as a function of delay time for pump and probe laser photon energies of $\omega_1 = 10.9$ eV and $\omega_2 = 16.3$ eV respectively. These photon energies and the delay times have been chosen to match those used in the pump-probe scheme of [15] where ionization from the $M = 0$ level was studied. Figure 1 shows that the dominant feature in the ionization probability is a fast oscillation with a period of approximately 0.29 fs. A closer look, however, provides signs of an additional slower oscillation. The amplitude of the fast oscillation is modulated by an oscillation with a period of around 0.8-0.9 fs. The fast oscillation has an amplitude of about 20% of the total signal. The slow oscillation is considerably weaker with an amplitude of about 5% of the total signal.

To analyse the ionization probabilities shown in figure 1 in more detail, we first look at the behaviour of the excited C$^+$ states populated by the pump pulse and then left to evolve freely. The pump pulse predominantly excites the lowest 2s2p^2 ^{2}D^e and ^{2}P^e states. The population of these states as a function of time are shown in figure 2. As these are eigenstates of the free atom, population transferred to these states by the pump pulse remains in these states after the pump pulse has completed. The figure therefore shows constant population of these states after the pump pulse. The population in LS-coupled states is thus insufficient to explain the oscillatory behaviour observed in figure 1. Figure 2 further shows that the greater detuning between the pump photon energy and transition energy to the 2s2p^2 ^{2}P^e excited state, compared

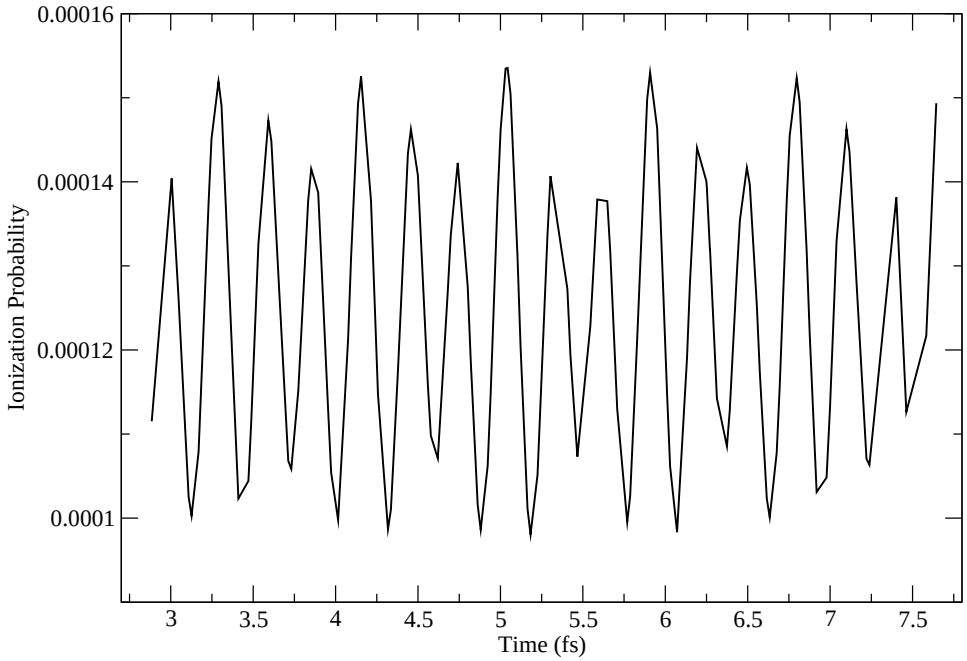

Figure 1. Ionization probability for C^+, initially in $M = 1$, given as a function of time elapsed between the beginning of the six-cycle 10.9 eV pump pulse and peak intensity of the six-cycle 16.3 eV probe pulse.

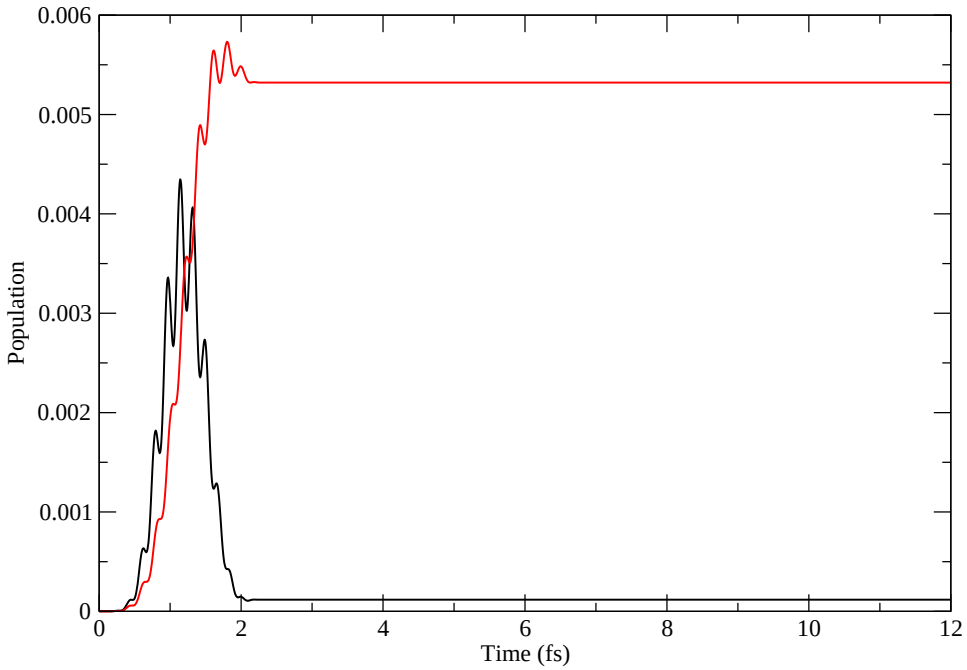

Figure 2. Populations of the 2s2p^2 ^{2}P^e (black) and ^{2}D^e (red) LS coupled states as a function of time, for a target irradiated by a six-cycle pump pulse of $\omega = 10.9$ eV and left to evolve freely. The start of the pump pulse is chosen at $t = 0$ fs.

to the 2s2p^2 ^{2}D^e state, results in a substantially smaller population in the ^{2}P^e state at the end of the pulse. During the pump pulse, the population of both states shows oscillations on top of an overall population (and depopulation) of the states. This demonstrates that both states are indeed excited directly from the ground state by the pump pulse.

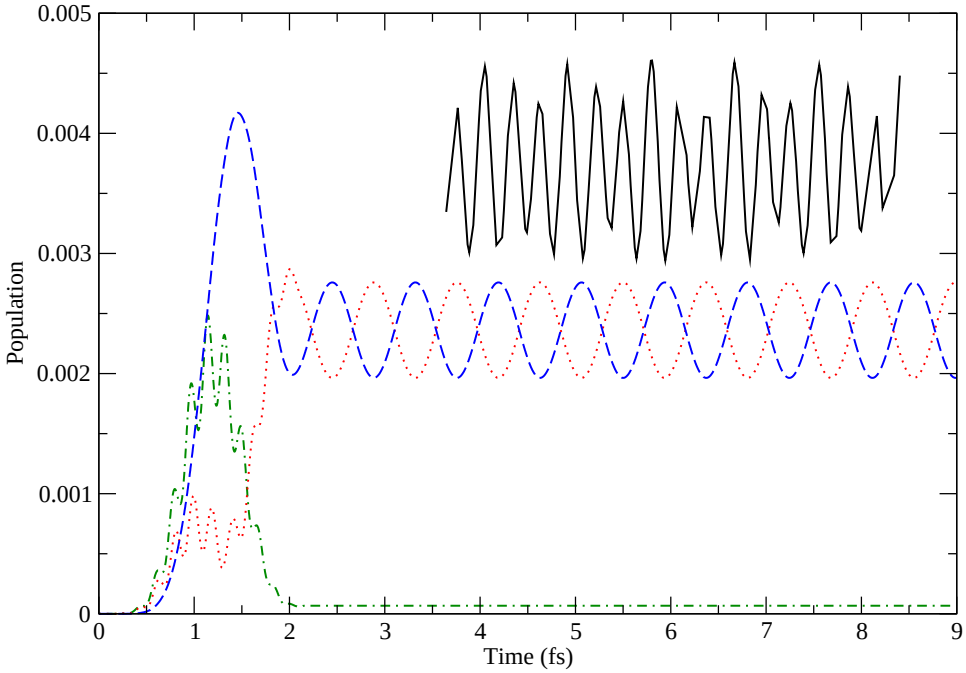

Figure 3. Populations of the $|\,0^-1^+0^+\rangle$ (dark green, dot-dash), $|\,0^+1^+0^-\rangle$ (red, dotted) and $|\,0^+1^-0^+\rangle$ (blue, dashed) states as a function of time. The ground-state C^+ ion, initially in the $M = 1$ level, is irradiated by a six-cycle pump laser pulse with photon energy $\omega = 10.9$ eV which starts at $t = 0$ and is then left to evolve freely. The ionization probability (black, solid) is given for comparison at a time corresponding to peak intensity of the six-cycle probe pulse. The ionization probability is scaled upwards by a factor of 30.

Following the same principles as used in the investigation of the dynamics in the 2s2p^2 configuration for $M = 0$ [15], the origin of dynamics may be more apparent if the uncoupled basis is used instead of the LS-coupled basis. Figure 3 thus shows the population in the $|\,0^-1^+0^+\rangle$, $|\,0^+1^+0^-\rangle$ and $|\,0^+1^-0^+\rangle$ states as a function of time. For comparison, figure 3 also provides the ionization probability given as a function of time elapsed between the start of the pump pulse and peak of the probe pulse. First of all, we can look at the evolution of the population in the uncoupled states during the pump pulse (0 to 2.3 fs). All three states show signs of population and depopulation. The populations of $|\,0^-1^+0^+\rangle$ and $|\,0^+1^+0^-\rangle$ show noticeable oscillations during this pulse, which indicates that these states can be populated directly by the pulse from the ground state. The population of $|\,0^+1^-0^+\rangle$ shows a much smoother behaviour, which indicates that this state cannot be populated directly by the pulse from the ground state. This is consistent with the discussion in section 3.2. Figure 3 further shows that the population $|\,0^+1^+0^-\rangle$ remains suppressed until near the end of the pump pulse, whereas there is a large initial increase in the population of $|\,0^+1^-0^+\rangle$.

$|\ 0^-1^+0^+\rangle$ receives initially a significant population, but this reduces considerably later due to the detuning of the pump pulse from the ^{2}P^e state excitation energy.

Following the end of the probe pulse, figure 3 shows a spin breathing motion between the populations of $|\ 0^+1^+0^-\rangle$ and $|\ 0^+1^-0^+\rangle$ with a period of approximately 0.87 fs. The physical effect in this breathing motion is an oscillation in electron spin between the $m = 1$ 2p electron and the $m = 0$ 2p electron. The period of the spin oscillation matches the period of the slow oscillation seen in the ionization probabilities. However, it is difficult to associate maxima in the ionization probabilities with specific characteristics of the spin oscillation, since these maxima do not correspond to a maximum in the population of either uncoupled state. Nevertheless the two quantities are in phase. The figure further shows that the magnitude of the spin oscillation is relatively small. Consequently, neither state is ever fully depleted and both states will always provide some contribution to the ionization process. This could account for the difficulty in observing the longer period behaviour in the ionization probability clearly.

The fast oscillations with a period of 0.30 fs do not appear to be directly linked to the population of $|\ 0^+1^+0^-\rangle$ or $|\ 0^+1^-0^+\rangle$. Similar fast oscillations were also observed in the previous study for magnetic quantum number $M = 0$ [15], and were ascribed to interference between the ground state and the excited states during ionization by the probe pulse. The fast oscillation in the present study also originates from this interference between ground and excited states. Comparison with published energy levels [22] for the 2s2p^2 ^{2}D^e and ^{2}P^e states suggests that interference between the ground state and each of these states should result in oscillations with periods 0.45 fs and 0.30 fs respectively. This indicates that the 2s2p^2 ^{2}P^e state plays an important role in the ionization process, as will be discussed later. The consequence of this fast interference, and its magnitude, is that effects due to spin dynamics cannot be observed from the ionization probability obtained using the present pump-probe scheme.

One of the outstanding questions from the previous study of the ionization probabilities [15] was the question whether electron-repulsion driven dynamics would be observable in the ionization probability for an unaligned initial C$^+$ ground state. We can combine the present ionization probability P_1 as a function of delay time, with those obtained previously for a C$^+$ ion initially in $M = 0$, P_0, to determine the ionization probability of an unaligned ground-state C$^+$ ion, $P_{\rm un}$:

$$P_{\rm un} = \frac{1}{3}P_0 + \frac{2}{3}P_1. \tag{12}$$

Figure 4 shows the ionization probabilities obtained for an unaligned C$^+$ ion as a function of time delay between the onset of the pump pulse and the peak of the probe pulse. The ionization probabilities for a ground-state C$^+$ ion initially in $M = 0$ [15] are provided for reference. For the unaligned ion, an oscillation with period of 1.5 fs, corresponding to the oscillation time between the $|\ 2p_02p_0\rangle$ and $|\ 2p_12p_{-1}\rangle_S$ states for a C$^+$ ion with $M = 0$, remains visible. However this oscillation is not as pronounced as it was; it has reduced in magnitude by a factor 3. Nevertheless, the oscillation still has an amplitude of 20-25% of the total ionization probability.

Although the ionization probabilities continue to provide evidence for electron-repulsion driven dynamics, more detailed information could potentially be gained from ejected-electron momentum distributions. These momentum distributions have previously been determined for C$^+$ ions initially in $M = 0$ [16], but for a probe pulse photon energy of 21.6 eV which allows the C^{2+} ion to be left in 2s2p ^{3}P^o. Here we

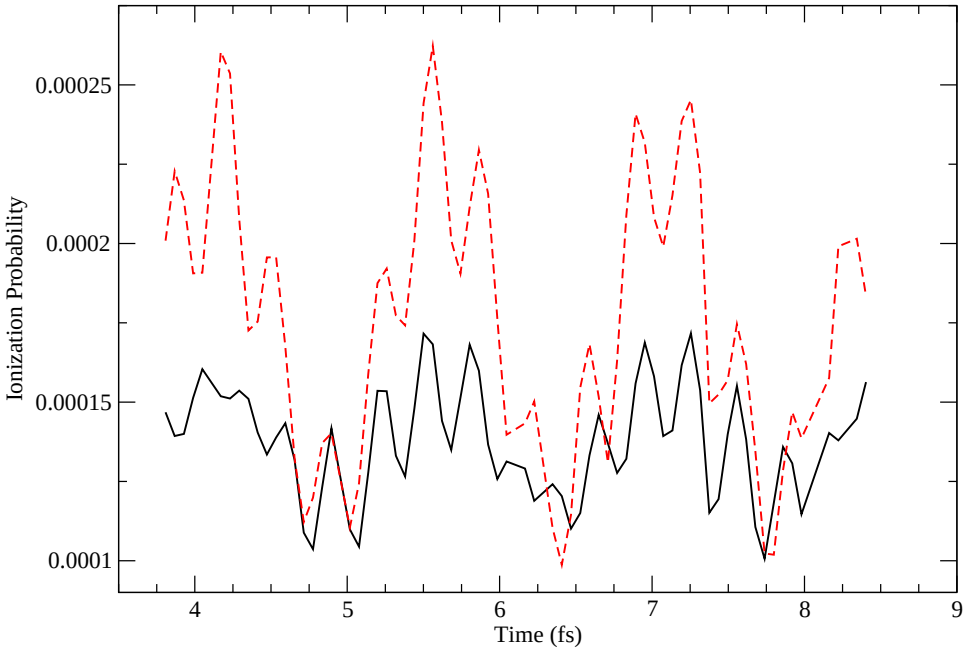

Figure 4. Ionization probabilities for ground-state C+ obtained using a six-cycle pump pulse of 10.9 eV and a six-cycle probe pulse of 16.3 eV as a function of time elapsed between the beginning of the pump pulse and the peak of the probe pulse. Ionization probabilities for an unaligned C^+ ion (black, solid line) are compared with those for a C^+ ion prepared in the $M = 0$ level (red, dashed line).

present momentum distributions for both $M = 0$ and $M = 1$ and for a probe pulse photon energy of 16.3 eV. This enables us to determine the momentum distribution for an unaligned initial C^+ ion as well. The ejected-electron momentum distributions for each initial value of M and the unaligned ion are compared at a time delay between the beginning of the pump pulse and the peak of the probe pulse of 5.65 fs in figure 5, chosen such that the ionization probability for $M = 0$ is at a minimum. The figure shows significant differences in the momentum distributions for the two initial values of M values, with the initial state with $M = 0$ predominantly leading to electron ejection along the axis of polarization, whereas the initial state with $M = 1$ primarily lead to emission perpendicular to the axis of polarization. Consequently, within the ejected-electron momentum distributions it is possible to distinguish between the contributions made by $M = 0$ and $M = 1$ in an unaligned C^+ ion. If we chose a time delay when the ionization probability for $M = 0$ is at a maximum, the contribution from the $M = 0$ process begins to dominate the unpolarized momentum distribution, however distinguishing the two processes is still possible. We note that while the shape of each momentum distribution is our primary interest, the magnitude of each momentum distribution in figure 5 differs. The maximum probability in the momentum distribution for $M = 0$ is approximately twice the maximum for $M = 1$, and about three times the maximum probability in the momentum distribution for an unaligned target.

The presence of sharp rings in the ejected-electron momentum distributions, shown in figure 5, indicates that ionization occurs primarily through the excitation of

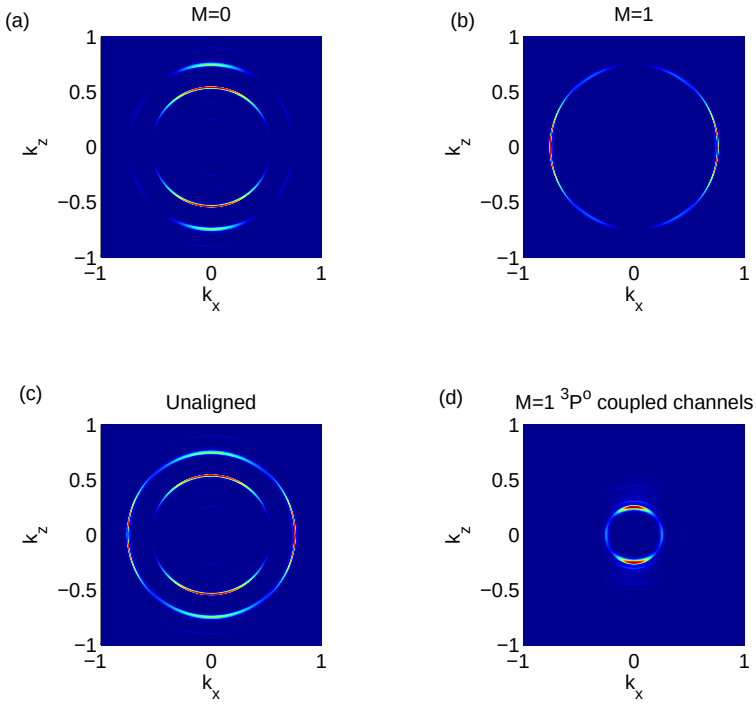

Figure 5. Ejected-electron momentum distributions for C^+ ions initially in the ground state obtained by irradiation by a six-cycle 10.9 eV probe pulse and a 16.3 eV probe pulse. The time elapsed between the beginning of the pump pulse and the peak of the probe pulse is 5.65 fs. The momentum distribution obtained leaving the residual C^{2+} ion in the $2s^2\ ^1S^e$ state are shown for $M = 0$ (a), $M = 1$ (b) and an unaligned C^+ ion (c). Also provided is the ejected-electron momentum distribution leaving the residual C^{2+} ion in the 2s2p $^3P^o$ state for $M = 1$ (d). Both pulses are polarized along the z-axis.

autoionizing resonances. This ring structure is present for both $M = 0$ and $M = 1$ and reveals important information about the ionization processes. The prominent ring in the ejected-electron distributions for $M = 0$ occurs at an absorption energy of 28.4 eV, with a secondary ring at an absorption energy of 32.2 eV. On the other hand, the prominent ring in the ejected-electron distributions for $M = 1$ corresponds to an electron ejected after absorption of an energy of 32.2 eV. This suggests that the dominant ionization mechanism for $M = 0$ is absorption of a pump-pulse photon and a probe-pulse photon, whereas the dominant ionization mechanism for $M = 1$ is absorption of two probe-pulse photons. The second ring present in the ejected-electron momentum distributions for $M = 0$ at an absorption energy of 32.2 eV indicates that absorption of two probe-pulse photons also plays a role for this initial value for M. An examination of available final states [22] suggests that a good candidate for the autoionizing final state dominant in the $M = 0$ spectra is $2s2p(^1P^o)3s\ ^2P^o$. Excitation of this state from $2s2p^2$ would require one of the two 2p electrons to have $m = 0$. Thus

this state would be reachable when both 2p electrons have $m = 0$, but would not be reachable when one has $m = 1$ and the other $m = -1$.

The evaluation is not as straightforward for $M = 1$. Further analysis of the dominant ring in the $M = 1$ momentum distributions shows that the emission involves emission of both p and f electrons, although the emission of p electrons dominates. In addition, the probe pulse has a photon energy which is nearly resonant with the transition between the ground state and the 2s2p^2(^{3}P^e) ^{2}P^e state. As a consequence, the probe pulse increases the population in the ^{2}P^e state, whereas the population in the ^{2}D^e state is affected to a much lesser extent. The dominant ring in the ejected-electron momentum distributions is then ascribed to the 2s2p(^{1}P^o)3d/4s states, excited primarily through the 2s2p^2(^{3}P^e) ^{2}P^e state, and to a lesser extent through the 2s^{2}3d ^{2}D^e state. This explains the emission of both p and f electrons, with p electrons dominating, and the significantly weaker contribution of this process for $M = 0$. For $M = 0$, the 2s2p^2(^{3}P^e) ^{2}P^e state cannot be excited from the 2s^{2}2p ^{2}P^o ground state, since transitions with $\Delta L = 0$ are not allowed.

The final-state energy of the two-photon ionization process in which two probe pulse photons are absorbed lies above the 2s2p ^{3}P^o state of C^{2+}. We should thus also consider ejected-electron momentum distributions associated for this final ionic state. Figure 5 shows the momentum distribution for $M = 1$: it again consists of a sharp ring, but with a substantially smaller value for the momentum of the ejected electron. For this final state, the emission of $m = 0$ electrons becomes allowed for $M = 1$ as demonstrated by the non-zero probability for emission of electrons along the polarization axis. In contrast to the 2s^2 ^{1}S^e state, 2s2p ^{3}P^o can be left in $M = 1$.

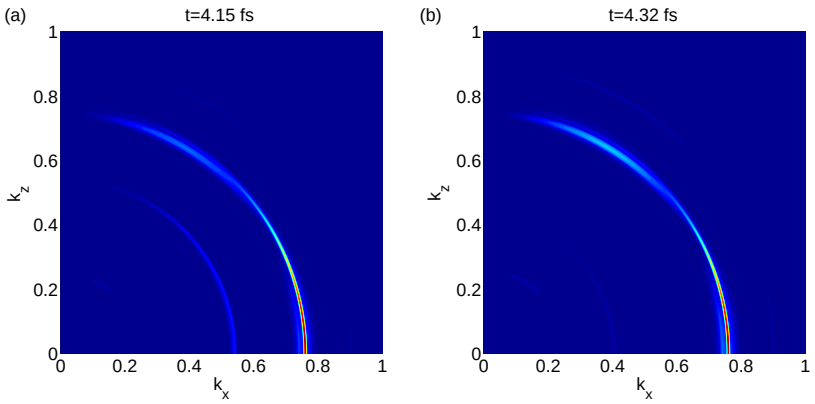

Figure 6. 2D momentum distributions calculated at elapsed times corresponding to peak intensity of the probe pulse at $\delta t = 4.15$ fs (a) and $\delta t = 4.32$ fs (b) for C$^+$ initially in the ground state with $M = 1$. The ion is irradiated by a six-cycle pump pulse with a photon energy of 10.9 eV and a six-cycle probe pulse of 16.3 eV. Time is measured from the beginning of the pump pulse.

The ejected-electron momentum distribution shown for $M = 1$ in figure 5 varies qualitatively with respect to the delay between the pump and probe laser, however. Whereas figure 5 shows a single ring in the momentum distributions, a second ring associated with a lower energy process periodically becomes significant enough to be noticeable. This is demonstrated in figure 6. This second process again occurs at a

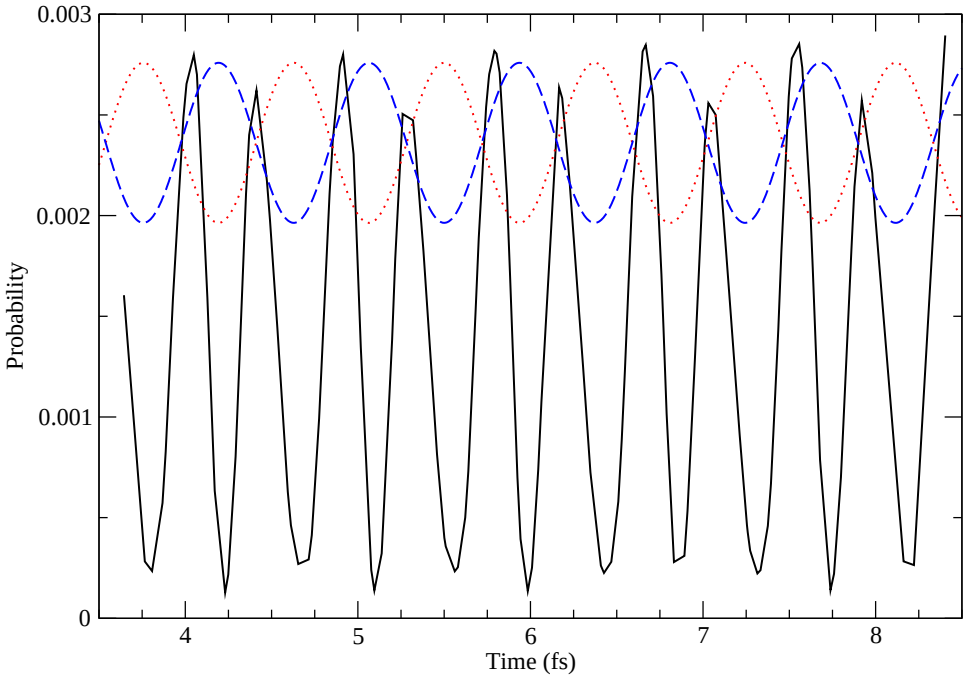

Figure 7. Variation in the probability of emission at E= 28.4 eV (black, solid), obtained by integrating the relevant ring in the momentum distribution over all angles and scaled upwards by a factor of 240, as a function of time. Time is taken as the time elapsed from the beginning of the pump pulse, with momentum distributions corresponding to the peak intensity of the probe pulse. Provided for comparison are the populations of the $\mid 0^+1^+0^-\rangle$ (red, dotted) and $\mid 0^+1^-0^+\rangle$ (blue, dashed) states.

distinct energy: E= 28.4 eV above the C^+ ground-state energy. The most likely state involved is again the $2s2p(^1P^o)3s\ ^2P^o$ state. This energy corresponds much closer to the sum of the pump-pulse and probe-pulse photon energies. Thus, this emission ring may be much better suited to the investigation of dynamics within the $2s2p^2$ configuration than the dominant emission ring.

Further detailed analysis of the momentum distributions revealed that lower energy processes, such as ionization by two pump-pulse photons, are also possible. However, these processes have a small to negligible probability of occuring, with little variation in this probability over the range of time delays considered. As such we do not consider these processes significant.

The overall picture of the ejected-electron momentum distributions can thus be separated into four distinct features, each indicative of a different ionization process. For both $M = 0$ and $M = 1$ we observe two processes, one corresponding to the absorption of a pump-pulse photon and a probe-pulse photon and the other corresponding to the absorption of two probe-pulse photons. Due to the different momenta involved, these processes are easily distinguished for both $M = 0$ and $M = 1$. The process involving a pump-pulse photon and a probe-pulse photon is the process of most interest, as this emission process is the one influenced by dynamics in the $2s2p^2$ configuration. For this process, the residual C^{2+} ion must be left in $2s^2\ ^1S^e$. Thus

the ejected electron must have a magnetic quantum number $m = M$. This means that the emission of an $M = 0$ and an $M = 1$ electron can be distinguished due to the different angular distribution of the emission process. Thus to obtain information about dynamics in the 2s2p^2 configuration, we should study the ring occurring at a total absorbed energy of 28.4 eV in the momentum distributions in detail.

The variation in the strength of the secondary emission process measured at a time corresponding to peak intensity of the probe laser pulse is shown in figure 7. The emission process is repetitive with a period of about 0.9 fs, but within each cycle two peaks in the emission strength can be observed. Although it is difficult to see from the figure, the gaps between individual peaks are not exactly the same. Nevertheless, we see that the secondary ring reaches a maximum intensity when the populations of $\mid 0^+1^+0^-\rangle$ and $\mid 0^+1^-0^+\rangle$ are roughly equal, and a negligible contribution when either of these states has maximal population. This quantity thus shows dynamics which is periodic with the frequency of the spin dynamics within the 2s2p^2 configuration.

We can enhance the appearance of the momentum distributions linked to the dynamics in the 2s2p^2 configuration in a straightforward manner. If the pump-pulse intensity is increased by a factor 2 and the probe-pulse intensity is decreased by a factor 2, then the ionization probability associated with a two-photon process in which one photon is absorbed from the pump pulse and one from the probe pulse should not be affected. However, the ionization probability associated with a two-photon process in which two photons are from the probe pulse should be decreased by a factor 4. Thus, ionization processes affected by dynamics in the 2s2p^2 configuration should increase in importance. When the intensities were varied in this manner for $M = 0$ this was indeed the case, with the E= 28.4 eV signal unaffected by the change. When similar changes were made to the intensities of the pump and probe laser pulses with energies 10.9 and 16.3 eV respectively for $M = 1$, we found that the E=32.2 eV signal scaled quadratically with probe laser intensity as expected. For the E=28.4 eV signal however, simultaneously halving the pump pulse intensity and doubling the probe pulse intensity resulted in a doubling of the probability of this process occurring. This gives us a clear indication that the E=32.2 eV signal is a result of the absorption of two probe pulse photons, whereas the E=28.4 eV signal arises from two processes: (1) absorption of two probe-pulse photons and (2) absorption of a pump-pulse and a probe-pulse photon. The probe pulse thus plays a major role in the observations. The 2s2p^2 dynamics may thus become clearer when the intensity of the probe pulse is reduced.

So far, we have considered pump and probe laser photon energies of $\omega_1 = 10.9$ eV and $\omega_2 = 16.3$ eV respectively with the stated aim of comparing the dynamics of C^+ in initial states with $M = 0$, $M = 1$ and when unaligned. As discussed earlier however, these laser frequencies were chosen to enhance the visible dynamics in the $M = 0$ case, but result in a large detuning between the pump laser and the 2s2p^2 ^{2}P^e state as can be seen in figure 2. As a consequence, the population of the $\mid 0^+1^+0^-\rangle$ and $\mid 0^+1^-0^+\rangle$ states displayed an oscillatory behaviour, but neither state was fully depleted. Hence the dynamics for an $M = 1$ initial state may not be as pronounced at these frequencies, while correlations such as displayed in figure 7 may be coincidental. Thus, to obtain a better understanding of the $M = 1$ dynamics we consider a pump-probe scheme with a pump laser energy $\omega_1 = 11.5$ eV and a probe laser energy $\omega_2 = 15.7$ eV. These laser energies populate the 2s2p^2 ^{2}P^e and ^{2}D^e states in a similar fashion to figure 2, however the final populations of each state are now within approximately 30 % of each other after excitation by the pump pulse.

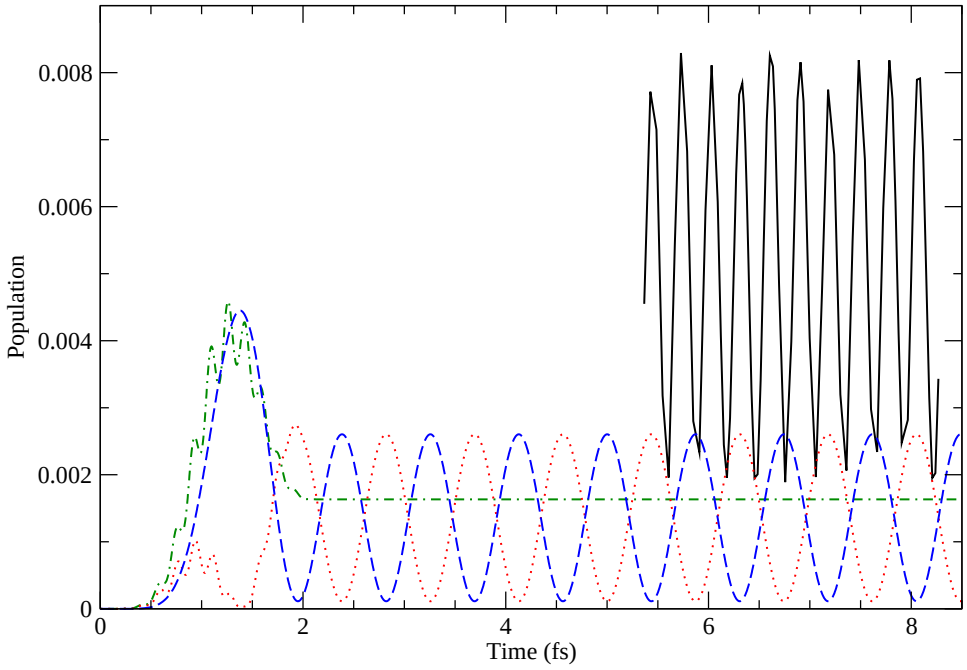

Figure 8. Ionization probability (black, solid), scaled upwards by a factor 30, for pump and probe photon energies of $\omega_1 = 11.5$ eV and $\omega_2 = 15.7$ eV respectively and measured at the time corresponding to peak intensity of the probe pulse. Time is measured from the beginning of the pump pulse. The $2s^2 2p$ initial state has magnetic quantum number $M = 1$. Also shown are the populations of each of $|\, 0^- 1^+ 0^+\rangle$ (dark green, dot-dash), $|\, 0^+ 1^+ 0^-\rangle$ (red, dotted) and $|\, 0^+ 1^- 0^+\rangle$ (blue, dashed) when excited by the pump pulse only and left to freely evolve.

The ionization probabilities, scaled upwards by a factor 30, for pump and probe laser photon energies of $\omega_1 = 11.5$ eV and $\omega_2 = 15.7$ eV are shown as a function of time in figure 8. We again observe an ultrafast oscillation with a period of 0.30 fs, which matches the oscillation observed earlier in figure 1. The oscillatory behaviour observed at these frequencies has two significant differences to our original frequencies however. Firstly, we note that the amplitude of the oscillation is much greater at these frequencies, despite the pump and probe pulses having the same combined energy in both cases. The ionization probabilities in figure 8 have a lower minimum value and a much higher maximum value than those displayed in figure 1, with peak values that are approximately 339% of the trough values where in figure 1 this difference was at most 56%. Secondly, we note that the long period behaviour in figure 1 is no longer present. So, there is no sign of spin dynamics within the $2s2p^2$ configuration in the ionization probabilities.

As before, the uncoupled basis provides more information about the dynamics of the wavepacket thus we consider the effects of the change in frequency on these states primarily. The populations of the uncoupled basis states $|\, 0^- 1^+ 0^+\rangle$, $|\, 0^+ 1^+ 0^-\rangle$ and $|\, 0^+ 1^- 0^+\rangle$ as a function of time when interacting with a pump pulse with photon energy $\omega_1 = 11.5$ eV are also shown in figure 8. For this frequency we see the same patterns that were observed in figure 3 for a pump photon energy $\omega_1 = 10.9$ eV, however after interaction with the laser pulse the final populations of each of

the uncoupled basis states show some significant differences. Firstly, we note that population of $|\ 0^-1^+0^+\rangle$ stabilizes again to a constant population but it is no longer so small as to be insignificant. This is a direct consequence of the increase in the population of the $^2P^e$ state, but as the population remains constant we do not expect $|\ 0^-1^+0^+\rangle$ to play any significant role in the time-dependent dynamics. As before, we expect the oscillation in the population of the $|\ 0^+1^+0^-\rangle$ and $|\ 0^+1^-0^+\rangle$ states to provide any possible link to variations in observable quantities. Significantly, the oscillatory breathing motion between the population of each of these states is now much more pronounced with transfer between the population of each being almost complete, leading to nearly complete depletion of $|\ 0^+1^+0^-\rangle$ or $|\ 0^+1^-0^+\rangle$. Comparison of the ionization probabilities and the population of the uncoupled basis states in figure 8 shows no significant relation between the two quantities

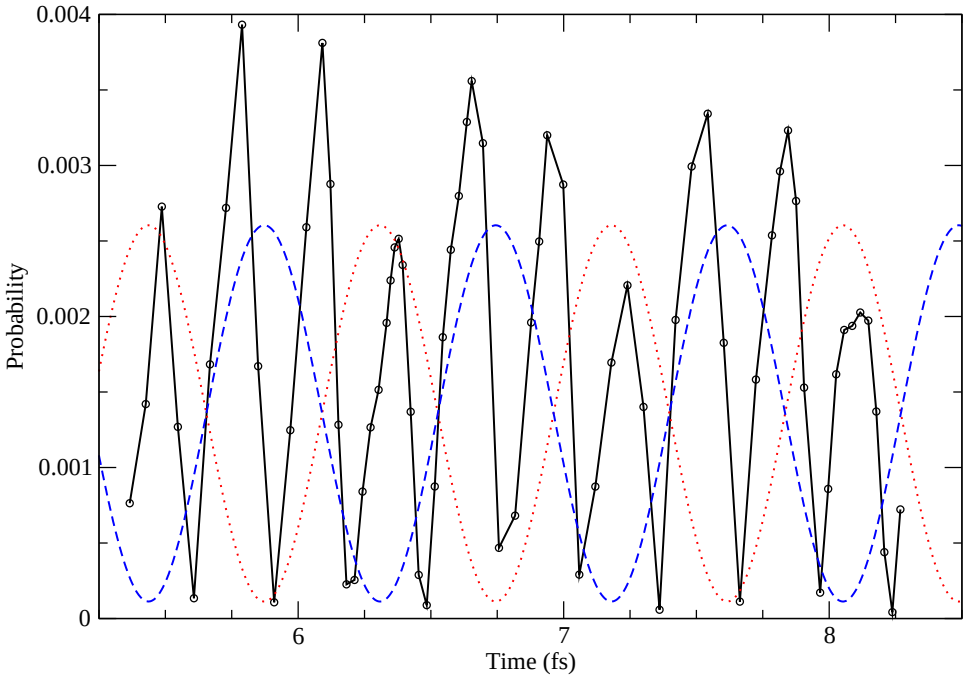

Figure 9. Variation in the probability of emission, scaled upwards by a factor of 120, at E= 28.4 eV (black) in the momentum distribution as a function of time for channels coupled to the $^1S^e$ target state for an initial state with $M = 1$. Provided for comparison are the population of the $|\ 0^+1^+0^-\rangle$ (red, dotted) and $|\ 0^+1^-0^+\rangle$ (blue, dashed) uncoupled basis states. Time is taken as the time elapsed from the beginning of the pump pulse, with momentum distributions corresponding to the peak intensity of the probe pulse.

The momentum distributions for these laser frequencies are very similar to our previous results shown in figures 5 and 6 with well-defined rings appearing at very specific ejected-electron momenta. However, we are particularly interested in the variation of the magnitude of the ring in the ejected-electron momentum distributions at an energy of E= 28.4 eV. The variation in the probability of emission from this ring for a pump laser photon energy of $\omega_1 = 11.5$ eV is shown in figure 9, along with the populations of the uncoupled basis states $|\ 0^+1^+0^-\rangle$ and $|\ 0^+1^-0^+\rangle$. The magnitude

of the momentum distribution peaks shows periodic behaviour on the timescale of the oscillations in the uncoupled basis states $|\ 0^+1^+0^-\rangle$ and $|\ 0^+1^-0^+\rangle$. Within each period for the uncoupled basis states $|\ 0^+1^+0^-\rangle$ and $|\ 0^+1^-0^+\rangle$, three peaks in the ionization probability are observed. Figure 9 shows that two peaks with a large, approximately equal, magnitude are followed by a peak which is about 30% smaller. This smaller peak occurs just after maximal population of $|\ 0^+1^+0^-\rangle$ is achieved.

The appearance of the smaller peak in the magnitude of the ring corresponding to an electron absorbing an energy of 28.4 eV coincides closely with maximum population in $|\ 0^+1^+0^-\rangle$. This can be explained as follows. The excitation from $2s2p^2$ to $2s2p(^1P^o)3s$ $(^2P^o)$ occurs through the $m = 0$ 2p electron absorbing a photon. This leaves opposite spin for the 2s electron and a 2p electron with $m = 1$. Hence, these can couple to singlet total spin. On the other hand, for $|\ 0^+1^+0^-\rangle$, this leaves parallel spin for the 2s electron and the 2p electron with $m = 1$. These electrons can not couple to singlet total spin, and the excitation process is thus not allowed. Thus we expect a reduction in the probability for excitation of $2s2p(^1P^o)3s$ $(^2P^o)$ when there is a maximum in $|\ 0^+1^+0^-\rangle$, and this is indeed what is observed in figure 9.

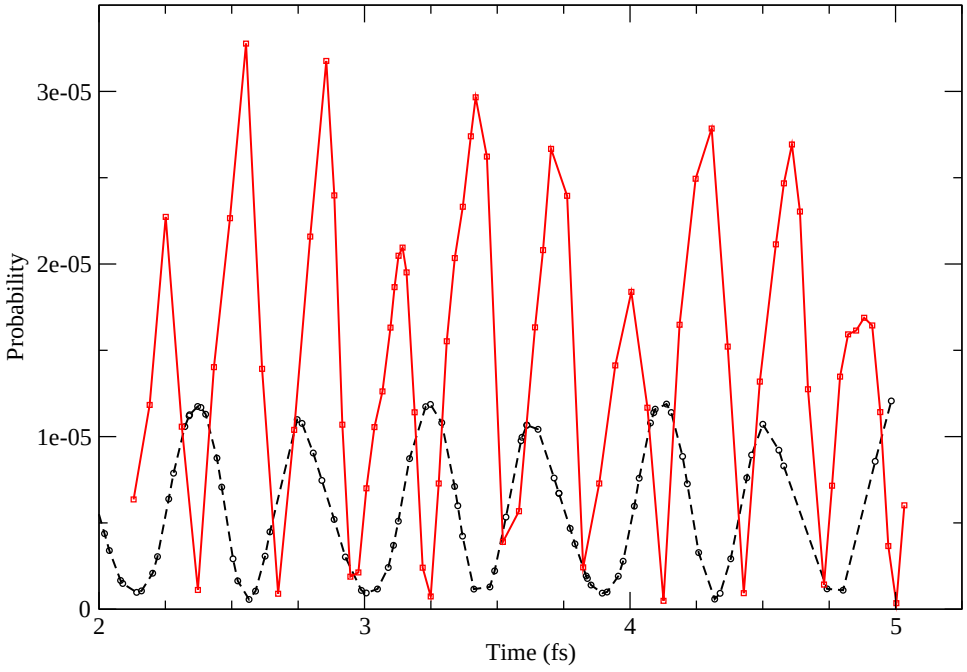

Figure 10. Variation in the magnitude of the E= 28.4 eV signal for pump laser energies of $\omega_1 = 10.9$ eV (black, dashed) and $\omega_1 = 11.5$ eV (red, solid) as a function of the time between the peak intensity of the pump pulse and the probe pulse.

The difference between the oscillations observed in figure 7 and those in figure 9 is best illustrated by comparing the results for each set of laser frequencies directly, as shown in figure 10. Direct comparison is achieved by considering the time elapsed between peak intensity of the pump and probe pulses. We see clearly that the smaller peak from figure 9 coincides with an irregularity in the oscillation observed in figure 7: the minimum at time $t = 3.0$ fs, $t = 3.9$ fs and $t = 4.8$ fs for $\omega_1 = 10.9$ eV is broader

than the minimum at intermediate times.

5. Conclusions

In the present report, we have continued the development of the time-dependent R-matrix approach by giving it the capability to study intense-field processes for atoms initially in a state with a total magnetic quantum number $M \neq 0$. The Hamiltonian is ordered by angular momentum, with alternating order of parity within each angular momentum to reduce the bandwidth of the Hamiltonian to two off-diagonal symmetries.

We demonstrate the TDRM method for $M \neq 0$ by investigating ultra-fast dynamics within the 2s2p^2 configuration of C$^+$ for $M = 1$. Analysis of the wavefunctions within this configuration shows that the ultra-fast dynamics within the 2s2p^2 configuration changes at a fundamental level with total magnetic quantum number M. Whereas the dynamics for $M = 0$ is entirely spatial dynamics, for $M = 1$ the dynamics is restricted to spin dynamics. This dynamics is a full three-electron dynamics, with the spin of the 2s electron acting as a flag for the presence or absence of spin dynamics between the two 2p electrons. Description of such dynamics thus requires a code capable of describing systems with more than two active electrons.

To investigate the ultra-fast dynamics within the 2s2p^2 configuration, we studied the response of ground-state C$^+$ to an ultrafast pump-probe scheme. The pump pulse excites C$^+$ to the 2s2p^2 configuration, while the probe pulse subsequently ionizes C$^+$ after a controlled time delay. Using a scheme designed to match a previous study for $M = 0$, we observe a fast oscillation in the ionization probability along with a weaker longer-period behaviour. The dominant ionization process is two-photon ionization through the 2s2p^2 ^{2}P^e state leading to an interference pattern due to excitation of this state either by the pump pulse or by the probe pulse. This interference leads to the fast oscillation in the two-photon ionization process. Evidence of spin dynamics within the 2s2p^2 configuration is more difficult to find. The effect on the ionization probabilities is in the order of 5-10%. Evidence for spin dynamics is more noticeable within the ejected-electron momentum distributions, but also these distributions are strongly affected by interference effects due to excitation of the 2s2p^2 configuration either by the pump or by the probe pulse. The clearest evidence for spin dynamics is observed for a pump-probe scheme involving photons of 11.5 and 15.7 eV respectively. The emission of electrons at an absorbed energy of 28.4 eV varies by 40% due to spin dynamics. Nevertheless, the effects of spin dynamics for C$^+$ with $M = 1$ are weaker than the effects of spatial dynamics in C$^+$ with $M = 0$.

By combining the results of the present calculations with those obtained previously for $M = 0$, we can also determine ionization probabilities and momentum distributions for unaligned C$^+$ ions. The large variation in the ionization probability observed for $M = 0$ is found to still be present for an unpolarized target, albeit at a reduced level: 20 - 25% of the total ionization probability. Direct comparison of the ejected-electron momentum distributions for C$^+$ ions with $M = 0$ and $M = 1$ initially demonstrate that the contributions from each process may be distinguishable in the momentum distributions obtained for an unaligned C$^+$ ion since these distributions have significantly different angular distributions.

Acknowledgments

SH was supported by the Department of Employment and Learning NI under the Programme for Government. MAL acknowledges funding under the HECToR distributed CSE programme, which is provided through The Numerical Algorithms Group (NAG) Ltd. HWH was supported by grant G/055816/1 from the UK Engineering and Physical Sciences Research Council.

References

[1] Kienberger R *et al.* 2004 *Nature* **427** 817
[2] Baker S *et al.* 2006 *Science* **312** 424
[3] Uiberacker M *et al.* 2007 *Nature* **446** 627
[4] Haessler S *et al.* 2010 *Nature Physics* **6** 200-206
[5] Schultze M *et al.* 2010 *Science* **328** 1658
[6] Lambropoulos P, Maragakis P and Zhang J 1998 *Physics Reports* **305** 203-293
[7] Parker J S, Doherty B J S, Taylor K T, Schultz K D, Blaga C I and DiMauro L F 2006 *Phys. Rev. Lett.* **96** 133001
[8] Mercouris Th, Komninos Y and Nicolaides C A 2007 *Phys. Rev. A* **76** 033417
[9] Guan X, Zatsarinny O, Bartschat K, Schneider B I, Feist J and Noble C J 2007 *Phys. Rev. A* **76** 053411
[10] van der Hart H W, Lysaght M A and Burke P G 2007 *Phys. Rev. A* **76** 043405
[11] Burke P G and Berrington K A 1993 *Atomic and Molecular Processes, an R-Matrix Approach*, (Institute of Physics Publishing Ltd., Bristol)
[12] Lysaght M A, van der Hart H W and Burke P G 2009 *Phys. Rev. A* **79** 053411
[13] Moore L R, Lysaght M A, Nikolopoulos L A A, Parker J S, van der Hart H W and Taylor K T 2011 *J. Mod. Optic.* **58** 1132-1140
[14] Lysaght M A, Burke P G and van der Hart H W 2008 *Phys. Rev. Lett.* **101** 253001
[15] Lysaght M A, Burke P G and van der Hart H W 2009 *Phys. Rev. Lett.* **102** 193001
[16] Lysaght M A, Hutchinson S and van der Hart H W 2009 *New J. Phys.* **11** 093014
[17] Lysaght M A and van der Hart H W 2010 *J. Phys. B: At. Mol. Opt. Phys.* **43** 121001
[18] Nikolopoulos L A A, Parker J S and Taylor K T 2008 *Phys. Rev. A* **78** 063420
[19] Smirnova O *et al.* 2009 *Nature* **460** 972
[20] Sukiasyan S, Patchkovskii S, Smirnova O, Brabec T and Ivanov M Yu 2010 *Phys. Rev. A* **82** 043414
[21] Hutchinson S, Lysaght M A and van der Hart H W 2010 *J. Phys. B: At. Mol. Opt. Phys.* **43** 095603
[22] Ralchenko Y, Kramida A E, Reader J and NIST ASD Team 2010 *NIST Atomic Spectra Database* (ver. 4), [Online]. Available: http://physics.nist.gov/asd3 [2011, June 3]. National Institute of Standards and Technology, Gaithersburg, MD